Electronic Supplementary Material (ESI) for Nanoscale.

Electronic Supplementary Information

Unprecedented carbon sub-microspheres with porous hierarchy for highly efficient oxygen electrochemistry

Yun-Pei Zhu[a] *and Shi-Zhang Qiao**[a,b]

[a] School of Chemical Engineering, The University of Adelaide, Adelaide, SA 5005, Australia.

[b] School of Materials Science and Engineering, Tianjin University, Tianjin 300072, China.

Correspondence to: s.qiao@adelaide.edu.au

1. Experimental Section

1.1. Materials synthesis

N,P-codoped hierarchically porous carbon nanospheres (NP-HPCS). In a typical run, 1.5 mmol of cetyltrimethylammonium bromide (CTAB) and 3.2 g of poly(acrylic acid) (PAA, average molecular weight 250 000, 35 *wt*% solution in water) were completely dissolved in a mixed solution of deionized water and ethanol (*v*/*v* = 10:1) under vigorous stirring at ambient temperature to form a homogeneous solution, followed by the dropwise addition of iminodi(methylphosphonic acid) (IMAP). After further stirring for 1 h, 3 mmol of ammonia was added into the above mixture. Then 15 mmol of phenol and 2.5 mmol of formaldehyde were added dropwise under tempestuously stirring. The clear solution was further stirred for another 2 h, followed by transferring to a Teflon-lined autoclave and aging statically at 80 ºC for 24 h. The polymeric product was collected by centrifugation, washed with water and ethanol alternatively, and dried in an oven at 50 ºC for 12 h, and then at 80 ºC for 12 h. The dried sample was treated in tubular furnace under the protection of nitrogen at 400 ºC for 2 h and then carbonized at 800 ºC for 2 h at a ramping rate of 2 ºC min^{-1}. Indeed, the organization of PAA and CTA^+ micelles through weak interactions, such as electrostatic interaction and hydrogen bonding could lead to the formation spherical complexes with ordered mesophase.[*Chem. Mater.* **2010**, *22*, 3829–3831.] Afterwards, the addition of organic precursors (phenol, formaldehyde, and IMAP) and the corresponding polymerization would trigger the reassembly of the mesomorphous PAA-CTA^+ complexes, wherein the organic polymers penetrated the ordered mesomorphous complexes and cross-linked around the orderly packed micelles to afford the well-ordered mesostructures.[*Chem. Lett.* **1999**, 1171–1172; *Chem. Soc. Rev.* **2013**, *42*, 3977–4003.] At the meantime, the weak interactions between PAA chains and the cationic surfactants were disturbed and/or disassembled and some PAA chains could disassociate from the ionic complexes to generate phase-separated PAA chain domains, which could actually perform as the templates for the interstitial nanopores inside the nanospheres after high-temperature carbonization.

P-doped hierarchically porous carbon nanospheres (P-HPCS). 1.5 mmol of CTAB and 3.2 g of PAA were dissolved in a mixed solution of deionized water and ethanol (*v*/*v* = 10:1) under vigorous stirring to form a homogeneous solution, followed by the dropwise addition of (hydroxyethylidene)diphosphonic acid (HEDP). After further stirring for 1 h, 3 mmol of ammonia was added into the above mixture. Then 15 mmol of phenol and 2.5 mmol of formaldehyde were added dropwise, and the clear solution was further stirred for another 2 h,

followed by transferring to a Teflon-lined autoclave and aging statically at 80 ºC for 1 d. The polymeric product was collected, washed, dried and finally treated in tubular furnace under the protection of nitrogen at 400 ºC for 2 h and then carbonized at 800 ºC for 2 h at a ramping rate of 2 ºC min^{-1}.

Pristine hierarchically porous carbon nanospheres (HPCS). The overall synthesis procedures are similar to those of chemically doped carbon counterparts but in the absence of organophosphonic acids.

1.2. Physicochemical characterization

Scanning electron microscopy (SEM) images were recorded on the FEI Quanta 450 at high vacuum with an accelerating voltage of 10 kV. Transmission electron microscopy (TEM) images and the selected area electron diffraction (SAED) pattern were obtained on a Philips CM200 microscope at an acceleration voltage of 200 kV. X-ray diffraction (XRD) pattern were collected on a powder X-ray diffractometer at 40 kV and 15 mA using Cu-Kα radiation (Miniflex, Rigaku). X-ray photoelectron spectra (XPS) were obtained using an Axis Ultra (Kratos Analytical, UK) XPS spectrometer equipped with an Al Kα source (1486.6 eV). Raman spectra were obtained on a WiTEC alpha300R Raman microscope with a 532 nm solid laser as an excitation source. N_2 adsorption-desorption isotherms were collected on a Quantachrome Autosorb-1 adsorption analyzer at 77 K. Prior to adsorption measurements, the samples were degassed at 200 °C in vacuum overnight. Pore size distribution curves were calculated using the adsorption branch of the isotherms by non-local density functional theory (NLDFT) method; surface areas were obtained by the Brunauer-Emmett-Teller (BET) method using adsorption data at a relative pressure range of P/P_0 = 0.05–0.30.

1.3. Electrochemical characterization

To prepare the working electrode, the synthesized carbon samples were first dispersed in a mixed solution containing 0.8 mL Mill-Q water and 0.2 mL isopropanol under sonication. 10 μL of the homogeneous catalyst suspension was transferred onto the glassy carbon rotating disk electrode (RDE, 5 mm in diameter) that was pre-polished with 0.5 μm down to 0.05 μm alumina powder, followed by coating a thin layer of Nafion solution onto the catalyst film and then dried under ambient conditions for 2 h. The resultant electrode were used as a working electrode during the electrochemical testing. All the electrochemical measurements were performed in a three-electrode configuration on a CHI 760D electrochemical workstation (CH

instrument Co., USA), wherein an Ag/AgCl (4 M KCl) and a graphite rod were respectively employed as the reference electrode and the counter electrode. The current density was normalized to the geometrical surface area, and all potentials were converted to a reversible hydrogen electrode (RHE) according to the Nernst equation ($E_{RHE} = E_{Ag/AgCl} + 0.205 + 0.059 \times pH$). A flow of O_2 was bubbled through the electrolyte (0.1 M KOH) during the recording of electrochemical measurements in order to assure the continued O_2 saturation. All the electrochemical data were recorded after contiguous cyclic voltammogram (CV) scans at a rate of 50 mV s^{-1} for at least 30 times. The Tafel slope was calculated according to Tafel equation as below:

$$\eta = b \cdot log(J/J_0)$$

where η, b, J, and J_0 represent overpotential, Tafel slope, current density, and exchange current density, respectively. On the basis of RDE data, the overall electron transfer number per oxygen molecule involved in oxygen reduction can be determined by Koutechy-Levich (K-L) equation:

$$1/J = 1/J_k + 1/J_L = 1/J_k + 1/B\omega^{1/2}$$

where J_k is the kinetic current and ω is the electrode rotating rate. B is determined from the slope of the K-L plots based on the Koutechy-Levich equation as given below:

$$B = 0.2nF(D_{O2})^{2/3}\upsilon^{-1/6}C_{O2}$$

where n represents the transferred electron number per oxygen molecule. F is Faraday constant (F = 96485 C mol^{-1}). D_{O2} is the diffusion coefficient of O_2 in 0.1 M KOH. υ is the kinetic viscosity. C_{O2} represents the bulk concentration of O_2. The constant 0.2 is adopted when the rotation speed is expressed in rpm.

For the ORR process, rotating ring-disk electrode (RRDE) voltammograms were carried out on an RRDE configuration (Pine Research Instrumentation, USA) with a 320 mm gap Pt ring electrode. The disk electrode was swept cathodically at a rate of 5 mV s^{-1} and the ring potential was constant at 1.5 V *vs.* RHE to efficiently oxidize any HO_2^- intermediate. The electron transfer number (n) and HO_2^- intermediate production percentage ($\%HO_2^-$) were determined as follows:

$$n = 4I_d/(I_d + I_r/N)$$

$$\%HO_2^- = 200I_r/(I_dN + I_r)$$

where I_d, I_r and N represent the disk current, the ring current and the current collection efficiency of the Pt ring which was determined to be 0.2.

1.4. Zn-air battery performance

For the Zn–air battery test, the mixed solution of 3 M KOH and 0.2 M $Zn(Ac)_2$ was used as the electrolyte, with a polished zinc plate as the anode. The air cathode was prepared through homogeneously coating the prepared catalyst ink onto a carbon fiber paper (Fuel Cell store), followed by drying at 60 ºC. Both electrodes were assembled into a Zn–air battery (2032 coin type) with a cellulose separator in between. For the cycling tests, one cycle consisted of one discharging step (5 mA cm^{-2} for 5 min) followed by one charging step of the same current density and duration time. The discharge polarization and power density (acquired by applying current density and measuring discharge voltage) plots were obtained using a galvanodynamic method with a current density ranging from 0 to 40 mA cm^{-2}.

2. Supplementary Figures

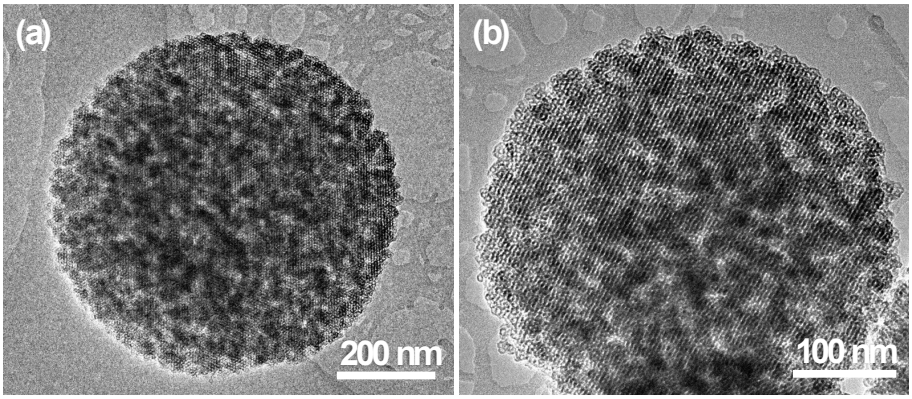

Fig. S1 TEM images of (a) P-HPCS and (b) HPCS. TEM images show the well-structured nanospheres with a size of approximately 600 nm for these two samples, which feature hierarchical porosity, *i.e.*, well-ordered mesopores with smaller pore size and larger interstitial nanopores.

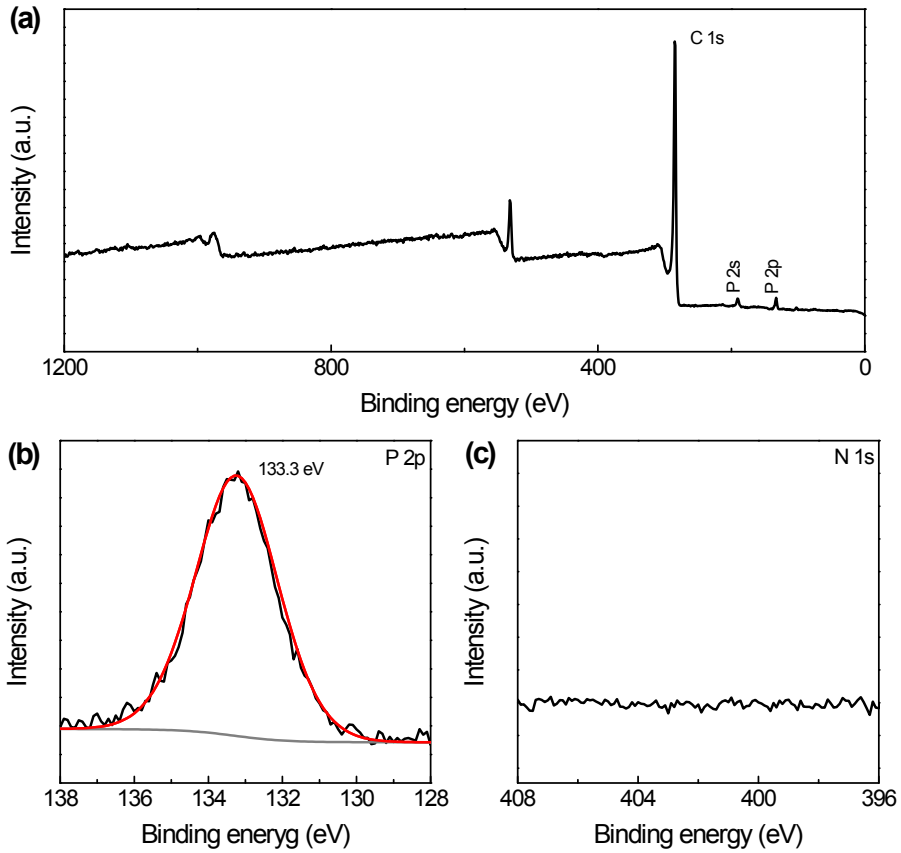

Fig. S2 (a) XPS survey scan, (b) P 2p and (c) N 1s core level for P-HPCS. The low-resolution XPS and high-resolution N 1s spectrum show the absence of N element, revealing that adjustment of organophosphonic acids with different functional groups is efficient in tuning the heteroatom genres in the resultant carbon frameworks. One symmetric peak situated at 133.3 eV in the P 2p region can be attributable to the P atoms chemically bonded to C or O atoms [*i.e.*, P–3C(–O)].

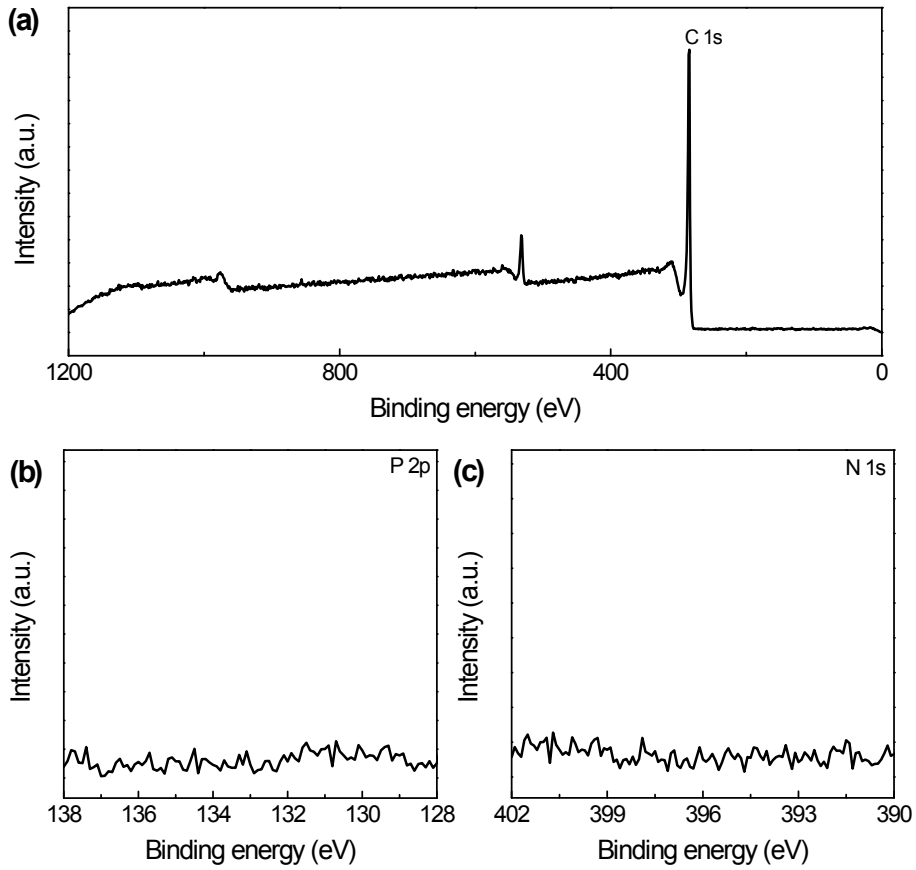

Fig. S3 (a) XPS survey scan, (b) P 2p and (c) N 1s core level for HPCS. The low-resolution and high-resolution XPS spectrum show that N and P elements are not detectable in HPCS which is synthesized in the absence of organophosphonic acids.

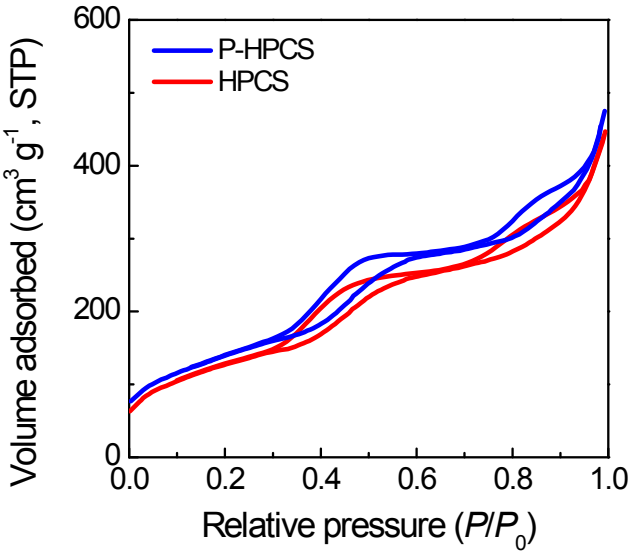

Fig. S4 N_2 adsorption-desorption isotherm of P-HPCS and HPCS. The adsorption-desorption isotherm of P-HPCS and HPCS, akin to that of NP-HPCS, are of type IV, accompanied with two distinct adsorption stages and hysteresis loops. The initial step at the relative pressure of 0.30–0.65 corresponds to mesopore with small pore size, while the second stage in the relative pressure region of 0.70–0.95 is related to the secondary interstitial pores with relatively large pore size, as observed by TEM imaging (Fig. S1). A significant increase of adsorbed nitrogen volume at even higher relative pressure can be attributed to the voids of the aggregated nanospheres and possibly larger secondary nanopores inside the nanospheres. Accordingly, the surface areas of P-HPCS and HPCS can be calculated to be 483 and 441 m^2 g^{-1}, respectively, supporting the case that introducing P dopants can effectively enhance the textural properties of the carbonaceous framework. [*J. Am. Chem. Soc.* **2009**, *131*, 5026–5027.]

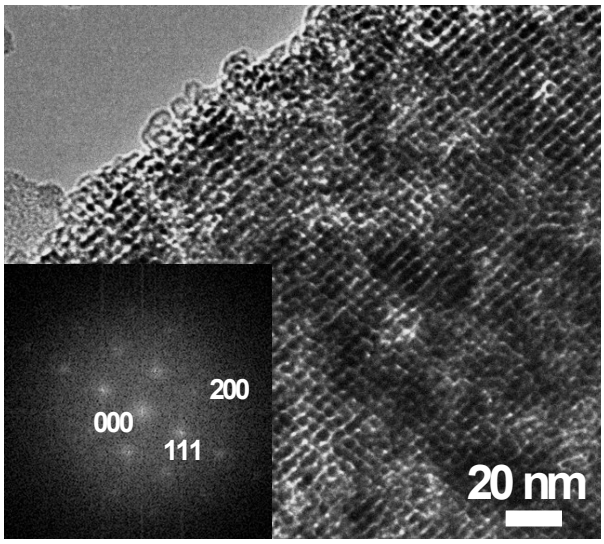

Fig. S5 TEM image of the NP-HPCS material. Inset displays the Fast Fourier Transformation (FFT) diffractogram.

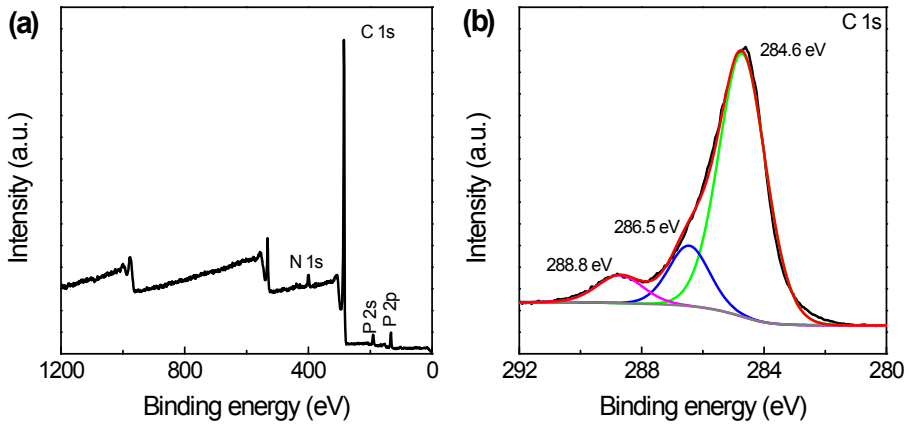

Fig. S6 (a) XPS survey spectrum and (b) high-resolution C 1s spectrum for NP-HPCS. The survey spectrum indicates that NP-HPCS contains N, P and C elements. The best deconvolution of the C 1s spectrum was achieved assuming the presence of three species, *i.e.*, sp^2-hybridized graphitic C (284.6 eV), N-sp^3 C (286.5 eV), and C=O (288.8 eV).

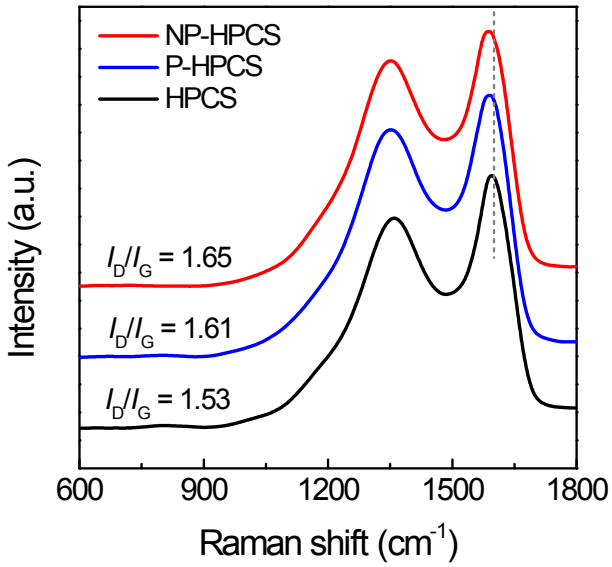

Fig. S7 Raman spectrum of the synthesized carbon materials. The two sharp signal peaks at low frequencies of around 1350 cm^{-1} and 1580 cm^{-1} correspond to D and G bands, respectively. As the G band is ascribed to tangential vibrations of graphitic carbon atoms, its presence is indicative of the existence of a graphitic structure in these carbon materials. In contrast, the D band, assigned to imperfections in sp^2 carbon structures, can be due to the presence of N and P dopants and the concomitant absence of graphitic carbon. It is noteworthy that the downshift of the G band for chemically doped carbon structures as compared with the pristine carbon provides additional evidence for the existence of defects induced by heteroatom doping.

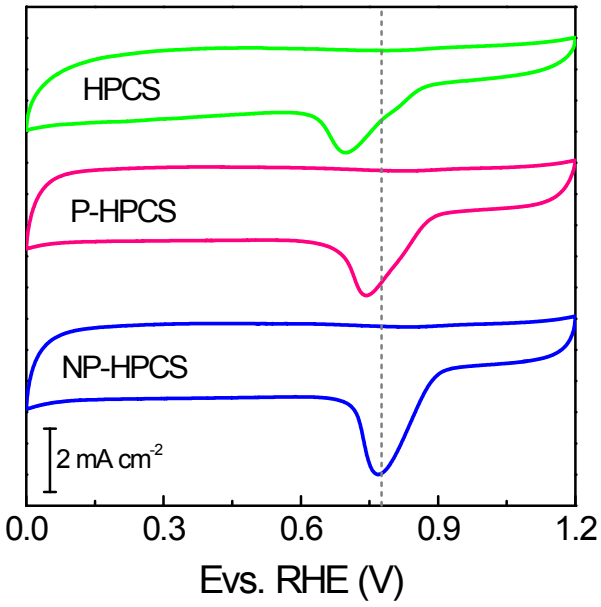

Fig. S8 CV curves of the synthesized carbonaceous electrocatalysts in an O_2-saturated 0.1 M KOH solution. It can be found that the oxygen reduction peak in CVs positively shifts for the case of NP-HPCS together with increased peak intensity as compared with P-HPCS and HPCS, indicating the positive role of dual doping in improving electrochemical activity.

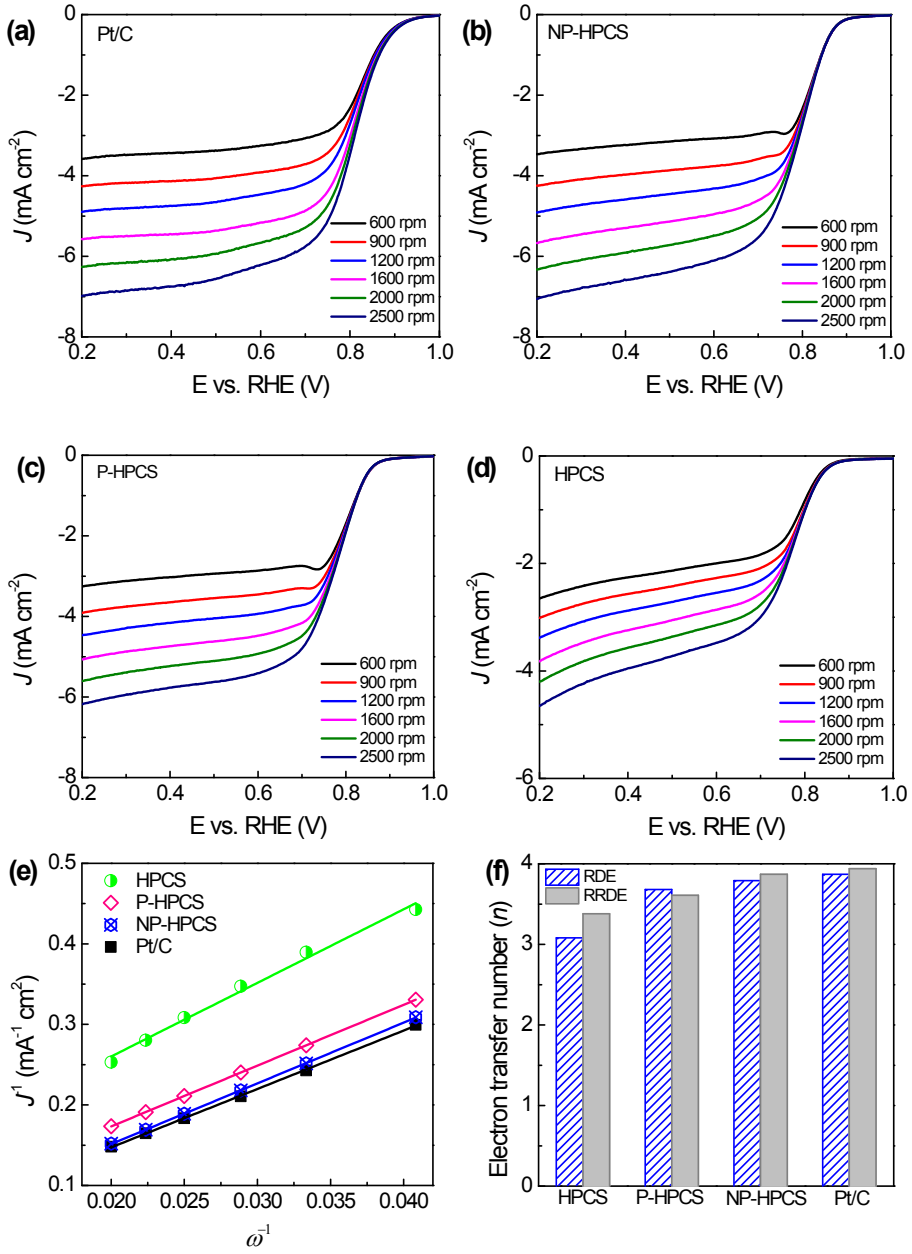

Fig. S9 (a-d) ORR LSV polarization curves of various electrocatalysts on RDE at different rotating speeds (600 to 2500 rpm) in O_2-saturated 0.1 M KOH solution. (e) K–L plots at 0.4 V based on the RDE curves. (f) The electron-transfer number per oxygen molecule (n) on the basis of RDE and RRDE results at 0.4 V.

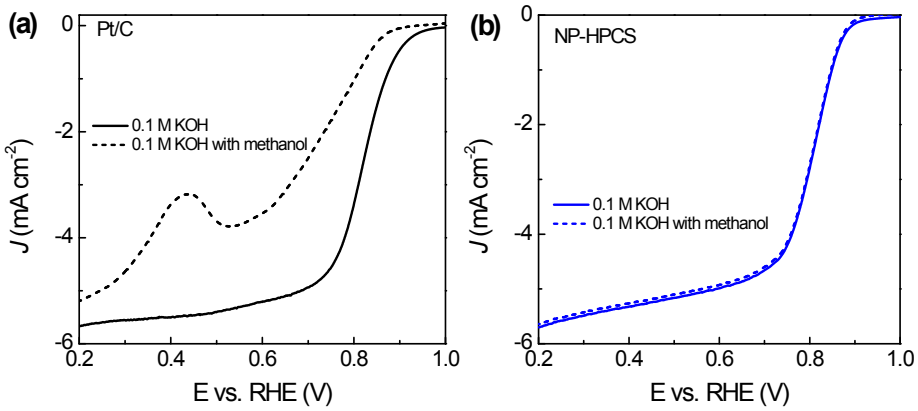

Fig. S10 Liner sweep voltammograms on RDE for (a) Pt/C electrode and (b) NP-HPCS electrode in O_2-saturated 0.1 M KOH with and without methanol at a rotating speed of 1600 rpm. The ORR curve for Pt/C electrode shows a weak oxidation peak between 0.4 and 0.6 V in the presence of methanol, which could be assigned to the oxidation of methanol. In addition, Pt/C electrode shows a negative on-set potential shift for ORR with the addition of methanol. In sharp contrast, no significant difference and/or change of the ORR curves can be detected for the NP-HPCS electrocatalyst in the presence of methanol, suggesting the excellent resistance towards methanol crossover effect.

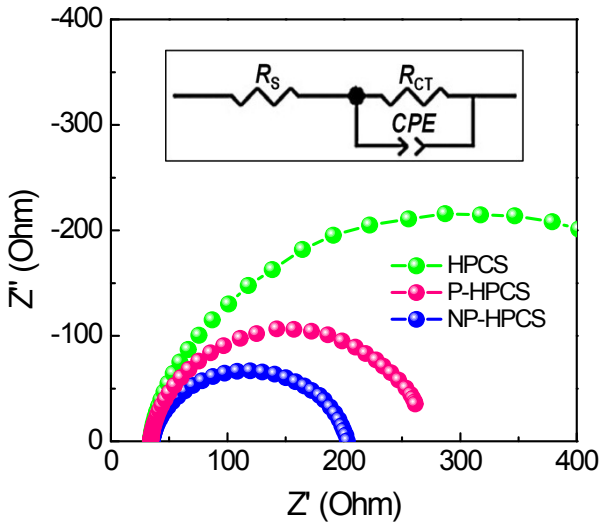

Fig. S11 Nyquist plots of EIS spectra of NP-HPCS, P-HPCS and HPCS. Inset shows the corresponding equivalent circuit. The semicircular diameter measured for NP-HPCS is much smaller than those of P-HPCS and HPCS, suggesting smaller contact and charge-transfer impedance induced by the synergistic effect of N and P doping, which are beneficial for the enhancement of electrocatalytic performance.

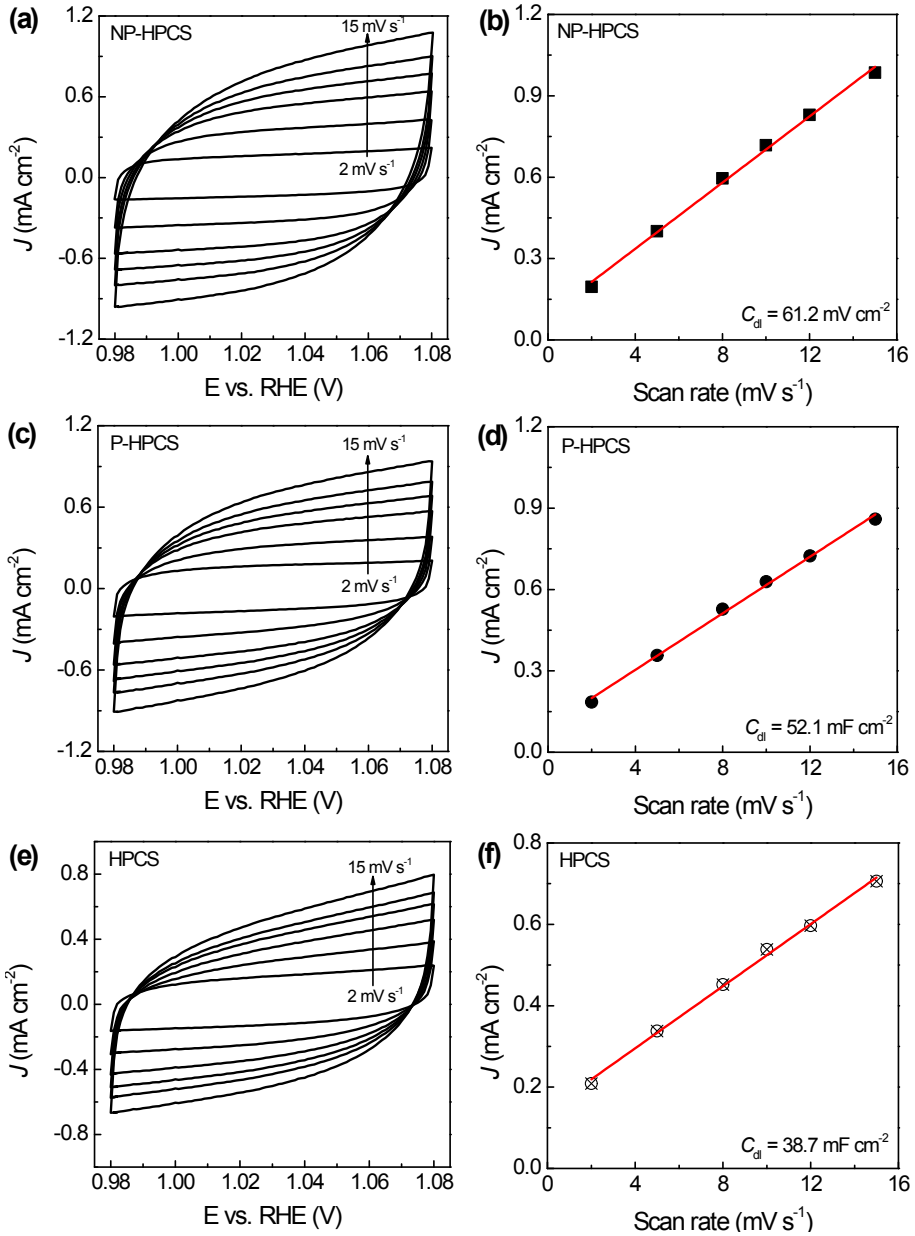

Fig. S12 CVs measured at different scan rates from 2 to 15 mV s^{-1} of NP-HPCS (a), P-HPCS (c) and HPCS (e). Plots of the current density at 1.06 V *vs.* the scan rate of (b) NP-HPCS, (d) P-HPCS, and (f) HPCS. CV curves display an approximate rectangular shape of an electrical double layer capacitor. In this potential region, the electrode reactions are considered to be negligible and the current originates solely from electrical double-layer charging and discharging. The plots of current density against the scan rate show a linear relationship, and the slope is the double layer capacitance (C_{dl} of NP-HPCS = 61.2 mF cm^{-2}, C_{dl} of P-HPCS = 52.1 mF cm^{-2}, and C_{dl} of HPCS = 38.7 mF cm^{-2}).

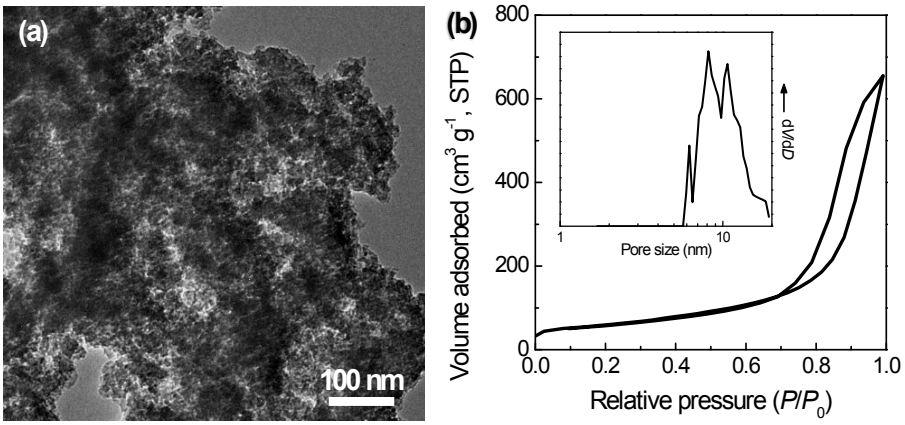

Fig. S13 (a) TEM image of NP-HPCS after ball-milling, demonstrating the loss of well-structured spheres and well-developed porosity. (b) N_2 adsorption-desorption isotherm of NP-HPCS after ball-milling. Inset shows the corresponding pore size distribution curve. The specific surface area can be determined to be 208 m^2 g^{-1}, much lower than that of NP-HPCS.

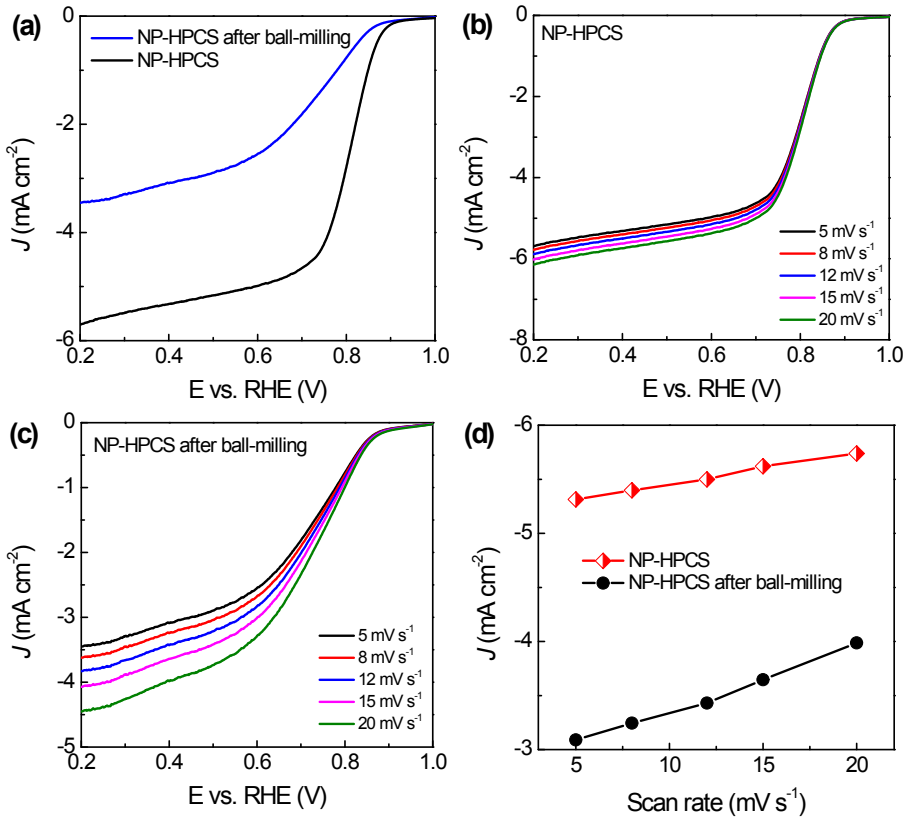

Fig. S14 (a) ORR LSV polarizations curves of NP-HPCS before and after ball-milling, showing much lower ORR electroactivity for the control sample after ball-milling in terms of onset potential and current density in comparison with NP-HPCS. LSVs recorded at a rotating rate of 1600 rpm at different scan rates for NP-HPCS (b) before and (c) after ball-milling. (d) A comparison of the plots showing the current density at 0.4 V *vs.* scan rate for NP-HPCS before and after ball-milling.

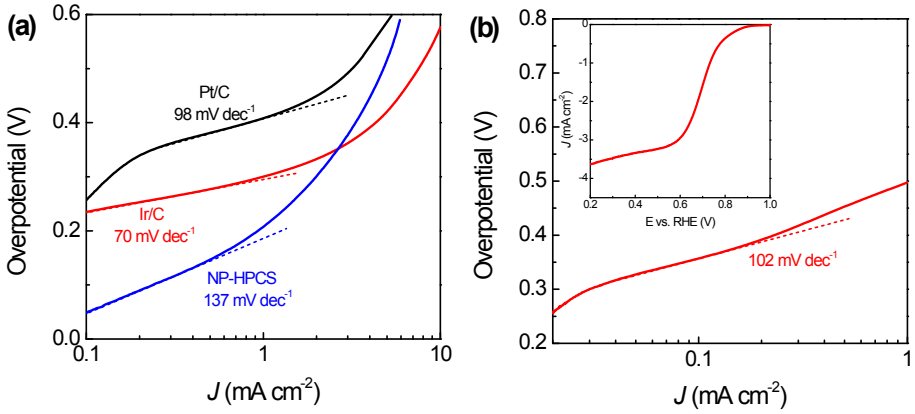

Fig. S15 OER Tafel plots of NP-HPCS, Pt/C and Ir/C. (b) ORR Tafel plot of Ir/C. Inset of (b) shows the corresponding ORR LSV polarization curve.

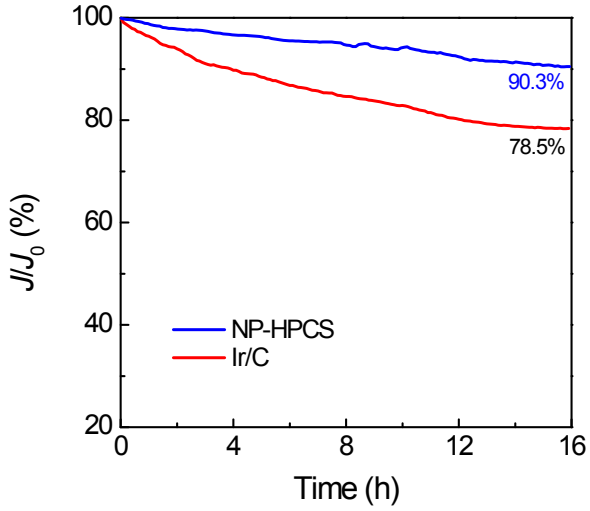

Fig. S16 Chronoamperometric responses of NP-HPCS and Ir/C towards electrochemical oxygen evolution, showing the superiority in long-term operation of NP-HPCS over the Ir/C benchmark.

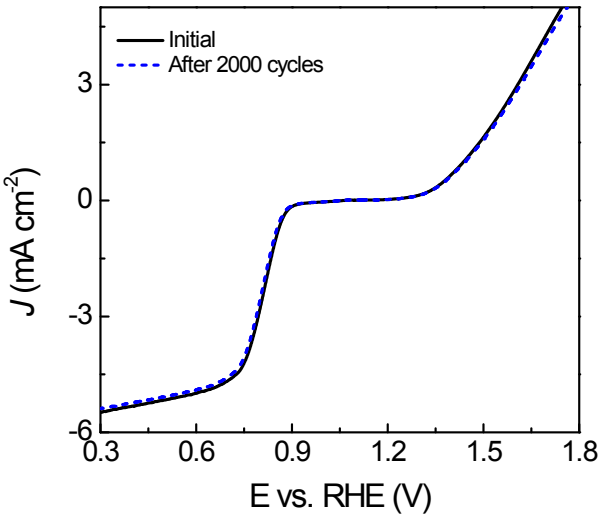

Fig. S17 LSV polarization curves of NP-HPCS in the whole ORR-OER region before and after 2000 cycling tests (O_2-saturated 0.1 M KOH, scan rate: 5 mV s^{-1}).

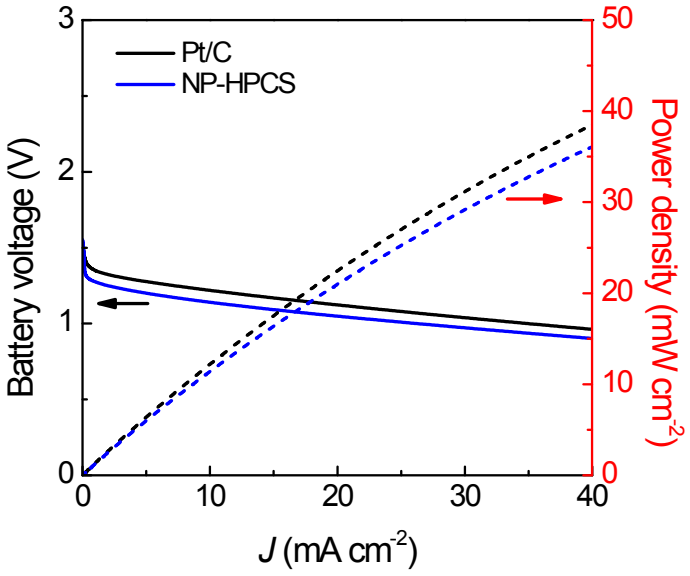

Fig. S18 Galvanodynamic charge curves and the corresponding power density profiles of air electrode bifunctional electrocatalysts, *i.e.*, NP-HPCS and Pt/C. The similar performance between these two electrocatalysts suggests the importance of dual doping and hierarchical architecture in boosting electrocatalytic oxygen reaction, as well as the potential for practical application in a real Zn-air battery.

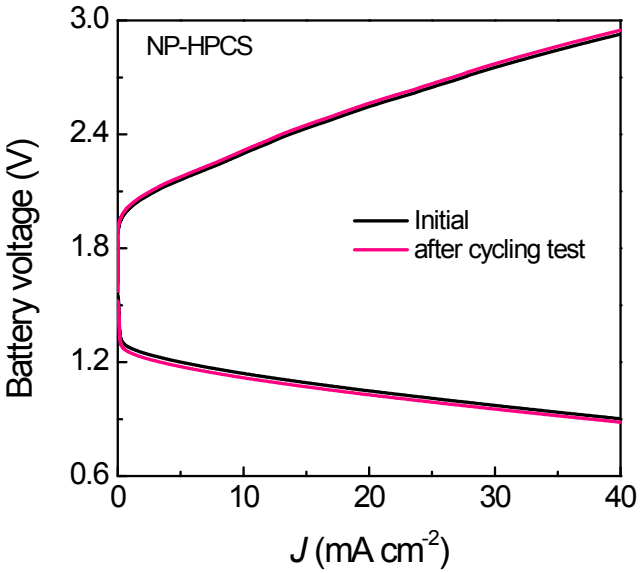

Fig. S19 Charge/discharge polarization curves of the Zn-air batteries using NP-HPCS as the air cathode before and after cycling test, showing no obvious change of the charge/discharge polarization curves before and after the cycling test.

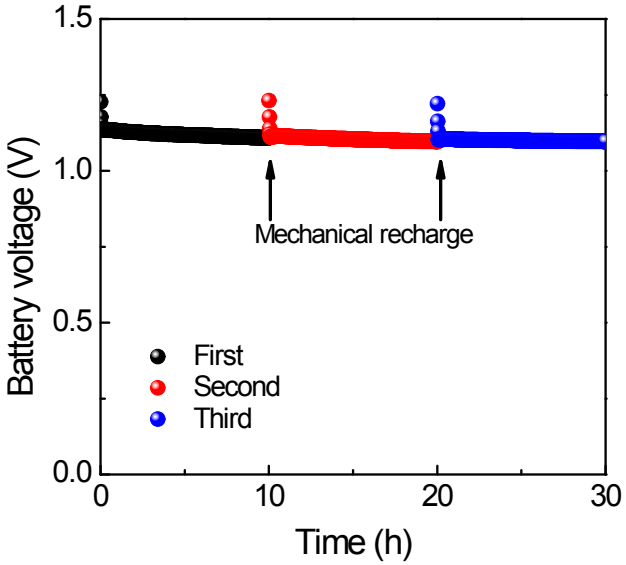

Fig. S20 Long-time durability of the Zn–air battery with the use of NP-HPCS electrocatalyst as the air cathode at a current density of 5 mA cm^{-2}. The corresponding performance of the Zn–air battery can be successfully regenerated for three consecutive runs, maintaining the similar performance over 30 h, which indicates the remarkable stability and mechanical rechargeability.

3. Supplementary Table

Table S1. Comparison of the electrocatalytic activity of recently reported bifunctional oxygen electrocatalysts.

Catalyst	*ORR*			*OER*		*Electrolyte*	*Substrate*	*Ref.*
	E_{onset}[a] /V	$E_{1/2}$[b] /V	*Tafel slope /mV dec^{-1}*	E_{onset} /V	*Tafel slope /mV dec^{-1}*			
NP-HPCS	0.92	0.82	72	1.30	137	0.1 M KOH	Glassy carbon	This work
P,S-g-C_3N_4 sponges	0.97	0.87	61	1.26	64	0.1 M KOH	Glassy carbon	S1
NPMC-1000	0.94	0.85	N.A.	N.A.	N.A.	0.1 M KOH	Glassy carbon	S2
N-doped graphene/ carbon nanotube	0.88	0.63	N.A.	1.50	83	0.1 M KOH	Glassy carbon	S3
N,S-porous carbon	0.99	0.85	58	N.A.	292	0.1 M KOH	Glassy carbon	S4
Egg-derived mesoporous cabon	0.84	0.69	N.A.	1.51	59	0.1 M KOH	Glassy carbon	S5
N,P,F-doped graphene	N.A.	N.A.	N.A.	1.62	136	0.1 M KOH	Glassy carbon	S6
N-doped graphene	0.90	0.81	53	N.A.	47	1 M KOH	Glassy carbon	S7
P-g-C_3N_4	0.94	0.67	122.3	1.53	61.6	0.1 M KOH	Carbon fiber paper	S8
N-doped carbon nanofiber film	0.97	0.82	N.A.	1.43	274	0.1 M KOH	N.A.	S9
Fe@N-doped carbon	0.96	0.83	N.A.	1.52	N.A.	0.1 M KOH	Glassy carbon	S10
Mn_xO_y/N-doped carbon	0.85	0.81	N.A.	1.55	82.6	0.1 M KOH	Glassy carbon	S11
N,Co-doped porous carbon polyhedron	0.97	N.A.	76	N.A.	292	0.1 M KOH	Glassy carbon	S12

[a] E_{onset}: onset potential *vs.* RHE. [b] $E_{1/2}$: half-wave potential *vs.* RHE.

4. Supplementary References

S1. S. S. Shinde, C. H. Lee, A. Sami, D. H. Kim, S. U. Lee and J. H. Lee, *ACS Nano*, 2017, **11**, 347–357.

S2. J. Zhang, Z. Zhao, Z. Xia and L. Dai, *Nat. Nanotechnol.*, 2015, **10**, 444–452.

S3. G. Tian, M. Zhao, D. Yu, X. Kong, J. Huang, Q. Zhang and F. Wei, *Small*, 2014, **10**, 2251−2259.

S4. Z. Pei, H. Li, Y. Huang, Q. Xue, Y. Huang, M. Zhu, Z. Wang and C. Zhi, *Energy Environ. Sci.*, 2017, **10**, 742−749.

S5. H. Wu, J. Geng, H. Ge, Z. Guo, Y. Wang and G. Zheng, *Adv. Energy Mater.*, 2016, **6**, 1600794.

S6. J. Zhang and L. Dai, *Angew. Chem. Int. Ed.*, 2016, **55**, 13296–13300.

S7. H. B. Yang, J. Miao, S. F. Hung, J. Chen, H. B. Tao, X. Wang, L. Zhang, R. Chen, J. Gao, H. M. Chen, L. Dai and B. Liu, *Sci. Adv.*, 2016, **2**, e1501122.

S8. T. Y. Ma, J. Ran, S. Dai, M. Jaroniec and S. Z. Qiao, *Angew. Chem. Int. Ed.*, 2015, **54**, 4646–4650.

S9. Q. Liu, Y. Wang, L. Dai and J. Yao, *Adv. Mater.*, 2016, **28**, 3000–3006.

S10. J. Wang, H. Wu, D. Gao, S. Miao, G. Wang and X. Bao, *Nano Energy*, 2015, **13**, 387−396.

S11. J. Masa, W. Xia, I. Sinev, A. Zhao, Z. Sun, S. Grützke, P. Weide, M. Muhler and W. Schuhmann, *Angew. Chem. Int. Ed.*, 2014, **53**, 8508–8512.

S12. Y. Hou, Z. Wen, S. Cui, S. Ci, S. Mao and J. Chen, *Adv. Funct. Mater.*, 2015, **25**, 872–882.